ELSEVIER

Contents lists available at ScienceDirect

Acta Materialia

journal homepage: www.elsevier.com/locate/actamat



Full length article

Lattice distortion in a strong and ductile refractory high-entropy alloy



Chanho Lee ^a, Gian Song ^b, Michael C. Gao ^c, Rui Feng ^a, Peiyong Chen ^a, Jamieson Brechtl ^d, Yan Chen ^e, Ke An ^e, Wei Guo ^f, Jonathan D. Poplawsky ^f, Song Li ^g, A.T. Samaei ⁱ, Wei Chen ⁱ, Alice Hu ^{g, h}, Hahn Choo ^a, Peter K. Liaw ^{a, *}

- ^a Department of Materials Science and Engineering, The University of Tennessee, Knoxville, TN, 37996-2100, USA
- ^b Division of Advanced Materials Engineering, Kongju National University, Cheonan, Chungnam, 330-717, Republic of Korea
- ^c National Energy Technology Laboratory/AECOM, Albany, OR, 97321, USA
- ^d Bredesen Center for Interdisciplinary Research and Education, The University of Tennessee, Knoxville, TN, 37996, USA
- ^e Chemical and Engineering Materials Division, Oak Ridge National Laboratory, Oak Ridge, TN, 37831, USA
- f Center for Nano-phase Materials Sciences, Oak Ridge National Laboratory, Oak Ridge, TN, 37831, USA
- g Department of Mechanical and Biomedical Engineering, The City University of Hong Kong, Kowloon, Hong Kong
- ^h Shenzhen Research Institute, The City University of Hong Kong, Shenzhen, PR China
- Department of Mechanical, Materials, and Aerospace Engineering, Illinois Institute of Technology, Chicago, IL, 60616, USA

ARTICLE INFO

Article history: Received 25 June 2018 Received in revised form 24 August 2018 Accepted 28 August 2018 Available online 30 August 2018

Keywords: Lattice distortion High-entropy alloy First-principles calculation In-situ neutron diffraction

ABSTRACT

The maximization of the mixing entropy with the optimal range of enthalpy in high-entropy alloys (HEAs) can promote the formation of a stable single solid-solution phase with the absence of competing intermetallic compounds. The resultant effects, such as lattice distortion, can contribute to excellent mechanical properties, which has motivated numerous efforts to develop and design single-phase HEAs. However, challenges still remain, particularly on quantifying the lattice distortion and relating it to materials properties. In this study, we have developed a NbTaTiV refractory HEA with a single bodycentered-cubic (BCC) structure using an integrated experimental and theoretical approach. The theoretical efforts include thermodynamic modeling, i.e., CALculation of PHAse Diagram (CALPHAD). The microstructural evolutions have been investigated by systematic heat-treatment processes. The typical dendrite microstructure was observed, which is caused by the elemental segregation during the solidification in the as-cast condition. The structural inhomogeneity and chemical segregation were completely eliminated by the proper homogenization treatment at 1200 °C for 3 days. The homogeneous elemental distribution was quantitatively verified by the Atom Probe Tomography (APT) technique. Importantly, results indicate that this HEA exhibits the high yield strength and ductility at both room and high temperatures (up to 900 °C). Furthermore, the effects of the high mixing entropy on the mechanical properties are discussed and quantified in terms of lattice distortions and interactomic interactions of the NbTaTiV HEA via first-principles calculations. It is found that the local severe lattice distortions are induced, due to the atomic interactions and atomic-size mismatch in the homogenization-treated NbTaTiV refractory HEA.

© 2018 Acta Materialia Inc. Published by Elsevier Ltd. All rights reserved.

1. Introduction

Novel metallic alloys beyond Ni-based superalloys with high strengths, thermal stabilities, and desirable ductility at high temperatures are highly desirable in the aviation and aerospace industries. To meet the increasing demand of elevated-temperature alloys, exotic multi-principal-element metallic alloy systems, also

* Corresponding author. E-mail addresses: pliaw@utk.edu, clee70@vols.utk.edu (P.K. Liaw). referred to as high-entropy alloys (HEAs), have been proposed and studied due to their simple microstructures and promising properties. The ideal HEA-design strategy is to form a single solid-solution phase, considering the configurational entropy (>1.5R, where R is the ideal gas constant), and the enthalpy of formation (ΔH_f) with the combinations of alloy components [1–8]_ENREF_1. The reduction of the Gibbs free energy by the high configurational entropy leads to the formation of the simple solid-solution phase, such as face-centered-cubic (FCC) [9], body-centered-cubic (BCC) [10–13], and hexagonal-close-packed (HCP) [14,15] structures.

These features, in turn, contribute to attractive materials properties, especially, high hardness/strengths, and excellent softening resistance at elevated and cryogenic temperatures [3–5]. These properties of the near-equimolar HEAs are known to be associated with the locally-strained atomic structures (lattice distortion) in the simple-single solid-solution phase. Moreover, the recently-developed twinning or transformation-induced plasticity (TWIP or TRIP) HEAs, whose compositions are greatly deviated from the near-equimolar ratios, have also attracted the increasing attention due to their excellent mechanical properties [1,5,16–25].

There have been extensive efforts to develop single-phase refractory HEAs for high-temperature applications above 1100 °C [10-13,26-28] and to comprehend the underlying relationship between their unique microstructure and mechanical performance. However, limited studies have investigated the lattice distortions in HEAs, using x-ray or neutron diffraction [29–31]. Furthermore, the quantitative evaluation of the lattice distortion, through statistical calculations with experimental observations, is still not fully developed. Moreover, only a small number of alloy systems have been verified as single BCC solid-solution phases from experiments [32,33]. For instance, many HEAs exhibit not only elemental segregations in the as-cast condition, but also the formation of small amounts of ordered phases after the heat treatment [27,34-36]. The chemical inhomogeneity and second-phase formation could hinder the fundamental and in-depth understanding of the main strengthening effect of HEAs. Therefore, the development of single solid-solution phase HEAs with homogeneous elemental distributions is vital to elucidate how lattice distortions affect mechanical properties. In the present study, we have designed a NbTaTiV refractory HEA, which contains a single BCC solid-solution phase, via the CALculation of PHAse Diagram (CALPHAD) approach [37–39]. The structure of the NbTaTiV alloy was investigated, using the integrated experimental and theoretical approach. The systematical heat treatments were conducted to develop the single-phase solidsolution microstructure with the fully-homogenous elemental distribution.

Furthermore, we investigated the lattice distortion and the local atomic environment of the BCC NbTaTiV alloy system through the *ab initio* method, based on Special Quasirandom Structures (SQS) [40] that approximate random distributions of atomic species in a medium-sized supercell. The fully-homogeneous single-phase NbTaTiV refractory HEA shows excellent yield strengths at room and high temperatures (up to 900 °C), which are mostly induced by the lattice distortion. The in-depth understanding of the lattice-distortion effect on mechanical properties gained through this investigation is expected to provide the alloy-design strategy for a significant step forward in obtaining the in-depth understanding of the refractory HEAs' microstructures and properties for high-temperature applications.

2. Experimental methods

2.1. Materials

The alloys were prepared from Nb, Ta, Ti, and V elements of 99.99 wt percent (wt.%) purity by vacuum arc-melting. Prior to each alloying, the chamber was evacuated to 10^{-5} torr. After the chamber pressure reached the desired value, the ultra-high purity argon gas was supplied to produce an arc beam. A Ti getter was used to consume traces of oxygen and hydrogen for all melting steps. To achieve a fully-homogeneous distribution of elements, the ingot was melted more than 10 times, by flipping them over between each step. From the master alloys, rods with a 4-mm diameter and 50-mm length were solidified in a Cu mold under the Ar atmosphere, followed by direct casting into cylindrical rods, using a

drop-casting technique. These fabricated alloys were sealed in the vacuumed (10^{-2} torr) quartz tube with the triple-pumped argon and experienced the heat treatments at $1000\,^{\circ}\text{C}$ for 1 day, $1200\,^{\circ}\text{C}$ for 1 day, and $1200\,^{\circ}\text{C}$ for 3 days. After that, the samples were water quenched.

2.2. Computational methodologies

The CALPHAD calculations were carried out, using the TCNI8 thermodynamic database supplied by ThermoCalc™ [41]. This database covers the entire composition ranges of all six constituent binaries of the Nb—Ta—Ti—V system. However, it is anticipated that the inclusion of thermodynamic descriptions for all ternaries will enhance the reliability of the database especially in applications for HEAs. Recent publications [37,38,42] detail the database developments and applications of the CALPHAD modeling for HEAs.

2.3. Microstructural characterization

Scanning-electron microscopy (SEM) was conducted, using a Zeiss Auriga 40 equipped with back-scattered electrons (BSE), and energy-dispersive X-ray spectroscopy (EDS). The SEM images were analyzed, using the ImageJ software [43] to obtain the volume fractions of dendrites and interdendrites, respectively. The surface morphology of the polished samples was studied by the electron-backscatter diffraction (EBSD) to indicate the presence of a single solid-solution phase and confirm the variation of the grain size and morphology after the heat treatment.

For the APT observation, needle-shaped specimens were made, using standard lift-out methods with an FEI Nova focused ion beam (FIB) [44,45]. The data collection was conducted, using a local electrode atom probe (CAMECA LEAP 4000X HR) equipped with an energy-compensating reflectron lens and a 10 pico-second 355 nm ultraviolet (UV)-pulsed laser. The specimen was cooled to 30 K, while a 50 pJ laser energy and a 200 kHz pulse repetition rate were used to evaporate ions with a detection rate of 0.005 ions per pulse. The data reconstruction and analysis were conducted, employing the IVAS 3.6.12 software (CAMECA instruments).

2.4. In-situ neutron-diffraction experiments

In-situ neutron-diffraction (ND) measurements of as-cast and heat-treated NbTaTiV alloys with a specimen diameter of 4 mm and length of 8 mm under compression were performed to investigate the deformation behavior at room temperature (RT), using an MTS load-frame on the VULCAN Engineering Diffractometer at the Spallation Neutron Source (SNS), Oak Ridge National Laboratory (ORNL) [46,47]. The ND instrument utilizes the time-of-flight (TOF) arrangement, which allows for the ND measurements with a diffraction pattern, covering a wide range of d spacings without the rotation of samples or detectors. The VULCAN is equipped with two detectors, designated as Banks 1 and 2 at \pm 90°. These two detectors were employed to record diffraction patterns corresponding to the lattice planes, which are parallel to the axial and transverse directions, respectively. The sample is illuminated by the incident neutron beam of a $3 \times 3 \text{ mm}^2$ slit size and 2-mm collimators. During the measurement of the diffraction patterns, a constant load-control mode with a stepwise-loading sequence was utilized. The measurement time of the neutron-diffraction data was 20 min at each stress level. When the stress level reached 1100 MPa (close to the yield strength), the control mode was changed from the load to displacement control modes with an incremental step of 0.2 mm. The collected data were analyzed by single-peak fitting, using the VULCAN Data Reduction and Interactive Visualization software (VDRIVE) program [48].

2.5. Mechanical tests

The mechanical experiments were carried out under uniaxial compression for the as-cast alloy at RT, as well as the heat-treated alloy at RT, 300 °C, 500 °C, 700 °C, 800 °C, and 900 °C, using a computer-controlled Material Test System (MTS) servo-hydraulictesting machine. It was very difficult to obtain high-quality specimens without the cast flaws, such as pores using copper-mold drop casting. Alternatively, further processes, such as rolling, are necessary to remove the flaws. Indeed, the secondary processing, i.e., rolling, seems to be quite effective to eliminate the micro-flaws formed during solidification. However, the microstructure, such as the grain size of samples after secondary processing, will be significantly changed or modified from that of the as-cast microstructure. It is believed that uniaxial compression is a possible method to obtain the intrinsic mechanical properties of as-cast and heat-treated NbTaTiV refractory HEAs. The experiments were conducted at an initial strain rate of 10^{-3} s⁻¹ with a specimen diameter of 4 mm and length of 8 mm (aspect ratio of 2:1). During the experiments at high temperatures, the test specimens were heated to the desired temperature by a furnace. Note that the mechanical test result is obtained from three to five repeated trials. All values of yield strengths and stress-strain curves are chosen as the representative data, which indicates the mean values of yield strengths. The repeated measurements of mechanical properties at elevated temperatures suggested that each set of tests show less than 8% deviation. The surface of the heat-treated specimen was polished to observe the surface-deformation morphology after 15% deformation.

2.6. First-principles calculations

The total-energy calculations were performed, using the Vienna *ab initio* simulation package (VASP) [49] based on the density functional theory (DFT) with the projector augmented wave (PAW) [50,51] method. The Perdew-Burke Ernzerhof (PBE) [52] function under the non-spin polarized generalized gradient approximation (GGA) interaction is used to describe the exchange and correlation interaction. The kinetic energy cutoff of 500 eV for the plane-wave basis is employed. Using the Monkhorst-Pack scheme, the Brillouin zone integration is carried out at $5 \times 5 \times 5$ k-points [53]. The convergence threshold for energy is 10^{-4} eV, while the symmetry-unrestricted optimization for the geometry is performed, employing the conjugate gradient scheme until the residual force on each atom is less than 0.01 eV/Å.

3. Results

3.1. Computational prediction of phase formation and evolution via the CALPHAD approach

The CALPHAD calculations were used to predict the microstructure of the NbTaTiV alloy. Fig. 1 shows the predicted equilibrium and non-equilibrium phase mole fraction versus temperature plots in the alloy system. A single BCC solid solution is predicted to form with the bulk composition of Nb23.8Ta25.5Ti24.9V25.8, atomic percent (at. %). The calculated liquidus and solidus temperatures are $T_{liq}\!=\!2161\,^{\circ}\text{C}$ and $T_{sol}\!=\!1941\,^{\circ}\text{C}$, respectively. The BCC solid solution decomposes into a minor HCP phase at $T_{dec}\!=\!432\,^{\circ}\text{C}$. The ratio of the temperature range where the BCC solid solution is stable over the solidus temperature [i.e., $(T_{sol}-T_{dec})/T_{sol}$] is determined to be 0.78. Gao et al. [54] previously proposed that a ratio greater than 0.30 typically favors a single-phase solid solution in the as-cast state.

The non-equilibrium solidification was simulated, using the

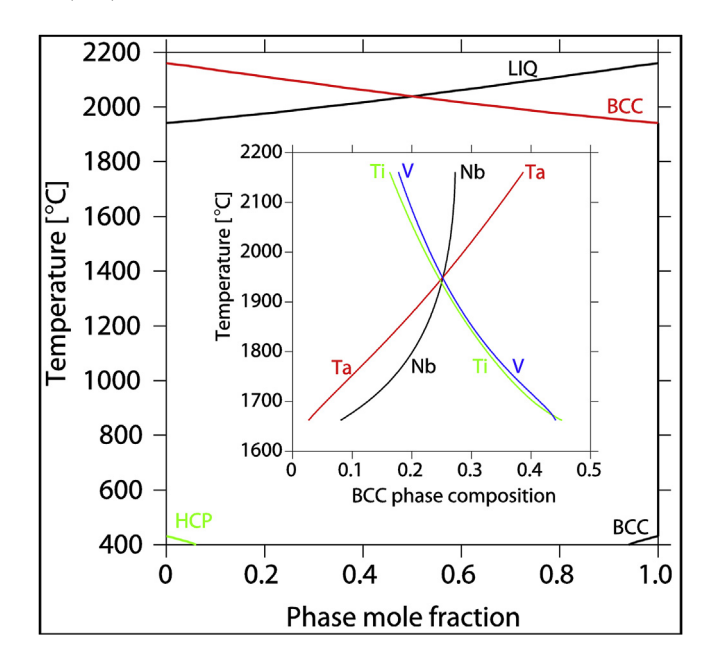


Fig. 1. CALPHAD-calculation data for NbTaTiV. Calculated equilibrium phase mole fractions during solidification for Nb $_{23.8}$ Ta $_{25.5}$ Ti $_{24.9}$ V $_{25.8}$. The inset shows the composition evolution of the BCC solid-solution phase during non-equilibrium solidification using the Scheil–Gulliver models.

Scheil-Gulliver model [55], which assumes equilibrium mixing in the liquid state and no diffusion in the solid state. The simulation predicts the formation of a single BCC solid solution during the entire non-equilibrium solidification. Based on the evidence, the real solidification path is thought to be somewhere between the equilibrium and Scheil-Gulliver model. The simulation also predicts the chemical segregation associated with Ta, Ti, and V due to constitutional cooling. It is believed that as the temperature decreases, the BCC phase is rich in Ta at earlier stages of solidification in the dendrite arms, while the interdendritic region is enriched in Ti and V in later stages (the inset in Fig. 1).

3.2. Chemical inhomogeneity in the as-cast sample

Fig. 2(a) shows the scanning-electron microscopy (SEM) back-scattered electron (BSE) image of the as-cast NbTaTiV refractory HEA. The microstructure consists of dendritic and interdendritic regions without any secondary phase. The different contrast between the dendritic and interdendritic regions suggests that elemental segregation occurs during the solidification process. The elemental distributions and chemical compositions of dendritic and interdendritic regions in the as-cast alloy were examined by the energy-dispersive-spectroscopy (EDS) mapping and point EDS analysis (not shown). The dendrite is enriched in Nb and Ta, while Ti and V are more preferentially distributed in the interdendritic region, which is consistent with the CALPHAD calculation in Fig. 1. The results of chemical compositions are summarized in Table 1.

The neutron-diffraction (ND) pattern in Fig. 2(b) reveals the formation of a single BCC phase without clear features related to the chemical segregation. Similarly, the EBSD-phase map in Fig. 2(c) shows the presence of a single BCC solid-solution phase. These results indicate that the ND and EBSD techniques can properly characterize the crystallographic-based microstructural features, such as the phase formation and grain size.

Atom probe tomography (APT) was performed to confirm the chemical homogeneity of the as-cast sample at the atomic scale and the composition of each region. Fig. 2(d) and (e) present elemental

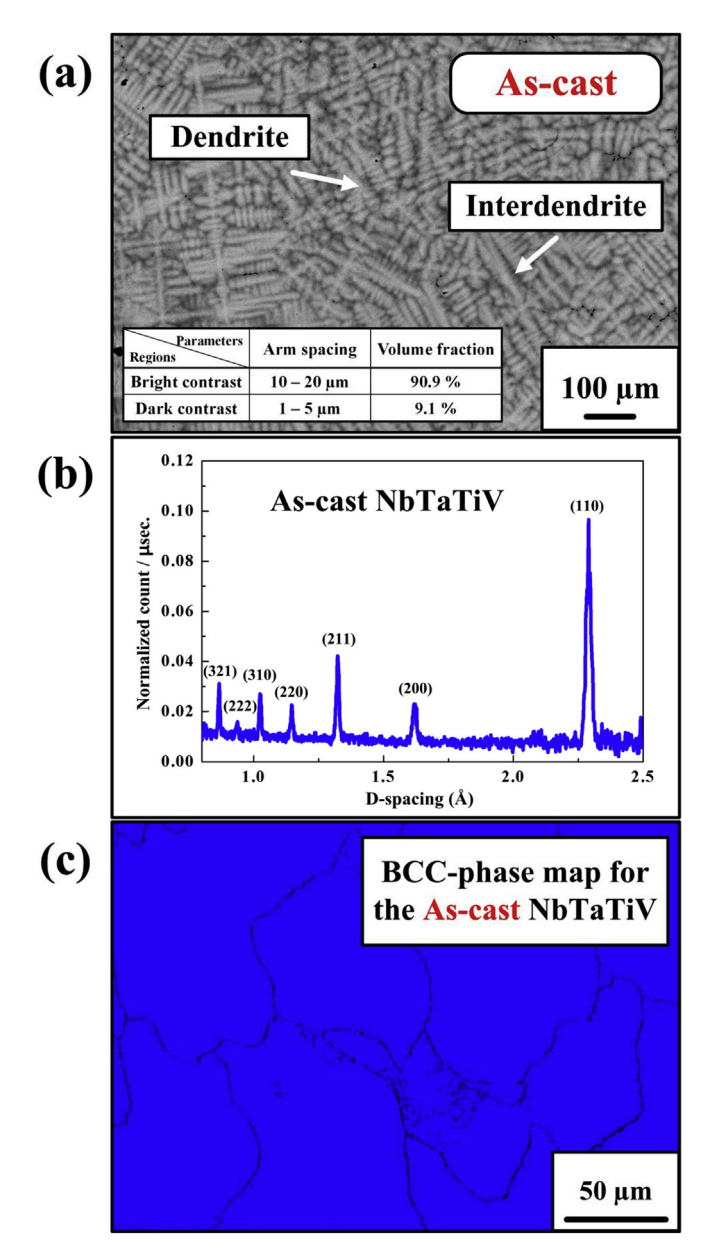


Fig. 2. Phase and microstructural characteristics of as-cast NbTaTiV, studied by SEM, ND, EBSD, and APT data. (a) The dendritic microstructure in SEM-BSE images of the as-cast NbTaTiV alloy (b) Neutron-diffraction patterns with the peaks indexed for a BCC structure (c) EBSD-phase map of the as-cast NbTaTiV alloy (d) Concentration-depth profile of all alloying elements taken along the black arrow (top), three-dimensional atom maps of individual elements (middle) and frequent-distribution histograms (bottom), for the dendritic region, and (e) Interdendritic region in the as-cast NbTaTiV alloy. The frequency-distribution histograms of constituent elements were calculated with a block size of 100 atoms with the solid lines showing the binomial-distribution curves, and the dots are the observed experimental results.

maps and one-dimensional concentration-depth data from the dendritic (bright contrast) and interdendritic (dark contrast) regions in analyzed volumes of $74 \times 71 \times 79 \text{ nm}^3$ and $81 \times 76 \times 114 \text{ nm}^3$ in the as-cast condition, respectively. The dendritic region was found to have a calculated composition of Nb 27.265, Ta 27.381, Ti 21.862, and V 22.150, at. %, while the interdendritic region had a calculated composition of Nb 20.997, Ta 11.669, Ti 33.149, and V 32.164, at. %.

The homogeneity of the atomic distributions within the APT dataset was evaluated via the chi-squared statistics using a frequency distribution analysis (FDA) [56], in which compositions from 100 ion bins of the observed data were compared to a binomial distribution, which represents a random solid solution. The

results of this analysis are presented in the inset of Fig. 2(d) and (e) with the experimental data (dots) overlaid on the theoretical binomial (random) distribution (solid line). The experimental results were in good agreement with the random binomial distribution, indicating random atomic arrangements within the atomprobe dataset. The μ value or χ^2 normalized to the sample size quantifies the extent of the elemental-distribution randomness. Only the μ value is reported in this case (see Table 1) due to the very large sample size, which causes the p test to be extremely sensitive to small variations. The μ value ranges from 0 to 1, with 0 indicating a complete random solid solution, and 1 representing a complete association of the elements. The χ^2 statistics applied to the APT data, including the μ value, are explained in more detail by Moody

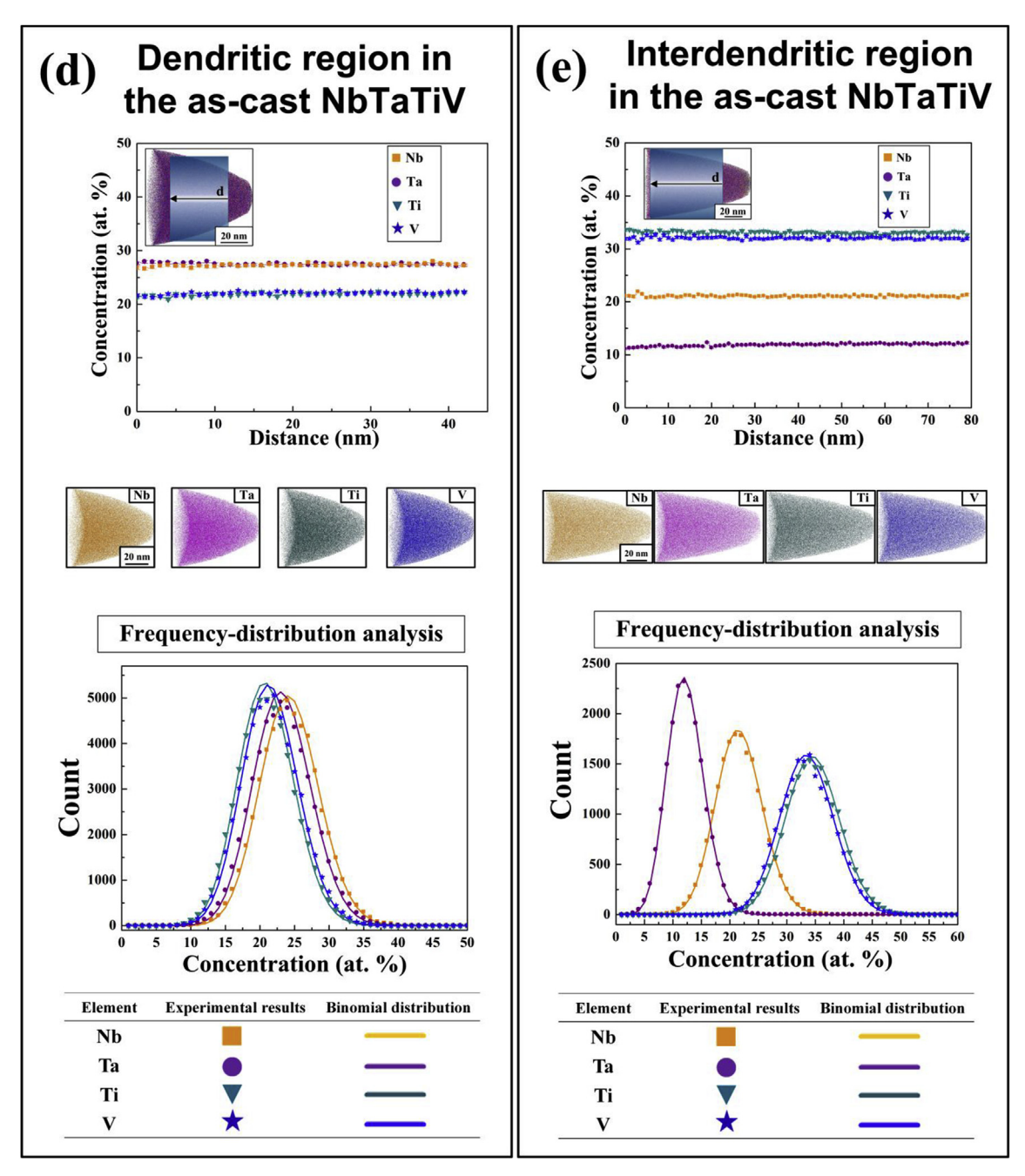


Fig. 2. (continued).

et al. [57] and Miller _ENREF_24_ENREF_24 [56]. One-dimensional concentration-depth profiles taken along a 10-nm cylindrical region further reflect that there are no statistically-significant concentration fluctuations in the dendritic and interdendritic regions, as shown in Fig. 2(d) and (e). However, there are clear chemical-composition differences between the two regions. The dendritic region contains higher amounts of Nb and Ta elements, whereas the interdendritic region consists of higher amounts of Ti and V, which are consistent with the EDS results (Table 1), and CALPHAD prediction (Fig. 1).

3.3. Tailoring single phase with homogeneous chemistry via thermal treatment

As an attempt to achieve a homogeneous single phase without

the compositional segregation in the as-cast alloy, systematic thermal treatments have been conducted, based on the CALPHAD results (i.e., heat treatments at 1000 °C for 1 day, 1200 °C for 1 day, and 1200 °C for 3 days). As the homogenization temperature and duration increase, an apparent microstructural variation is observed, as shown in Fig. 3(a–c). The dendrite-arm spacings and volume fractions of dendritic and interdendritic regions for the sample heat-treated at 1000 °C for 1 day are slightly larger [Fig. 3(a)] than those of the as-cast sample [Fig. 2(a)]. The quantitative difference of dendrite-arm spacings and volume fractions are summarized in each figure. This variation implies an insufficient diffusion at the above temperature. The heat treatment at 1200 °C for 1 day leads to the blurred contrast between dendrites and interdendrites [Fig. 3(b)], which indicates a gradual reduction of the compositional segregation.

Table 1 SEM-EDS and APT compositions, and elemental distribution analyses of as-cast and homogenization-treated refractory NbTaTiV HEAs. Chemical composition (in atomic percent, at. %) of constitutive regions in as-cast and homogenized alloys, determined using the energy-dispersive spectroscopy (EDS) and atom-probe tomography (APT), respectively. The binomial distribution of the analyzed data in comparison to the binomial distribution of the theoretical data is provided by the parameters of χ^2 and μ for each element

| Materials | Parameters | | | | | |
|----------------------------------|------------|------------------------------|------------------------------|--------|--|--|
| | _ | EDS results | APT results | | | |
| Alloys | Elements | Average of atom fraction (%) | Average of atom fraction (%) | | | |
| As-cast | Nb | 28.6 | 27.265 | 0.0564 | | |
| NbTaTiV (Bright contrast region) | Ta | 33.7 | 27.381 | 0.1029 | | |
| | Ti | 19.8 | 21.862 | 0.0779 | | |
| | V | 17.9 | 22.150 | 0.1014 | | |
| As-cast | Nb | 18.9 | 20.997 | 0.0422 | | |
| NbTaTiV (Dark contrast region) | Ta | 9.0 | 11.669 | 0.0390 | | |
| | Ti | 36.3 | 33.149 | 0.0586 | | |
| | V | 35.8 | 32.164 | 0.0664 | | |
| Homogenized | Nb | 23.8 | 24.944 | 0.0375 | | |
| NbTaTiV | Ta | 25.5 | 23.627 | 0.1328 | | |
| | Ti | 24.9 | 25.076 | 0.0820 | | |
| | V | 25.8 | 24.959 | 0.0379 | | |

To obtain a fully-homogeneous elemental distribution, the sample was subjected to a longer heat treatment at 1200 °C. This thermal treatment results in the complete elimination of the dendritic segregation concomitant with the grain growth (grain sizes of $200-400 \,\mu\text{m}$), as observed in Fig. 3(c). The EDS measurements (not shown) were conducted to further confirm the homogeneous chemical distribution in the sample heat-treated at 1200 °C for 3 days. No formation of other phases along the grain boundary as well as inside the grain was observed. The specific chemical composition for the homogenized microstructure was investigated by the point EDS analysis. Importantly, each element was distributed as a nearly-equi-atomic percentage throughout the sample. The results of chemical compositions are summarized in Table 1. The ND pattern and EBSD-phase map show that there is no obvious formation of the secondary phase or phase transformation after the heat treatment [Fig. 3(d) and (e)].

The atomic-scale distribution of elements for the homogenized sample was measured, using an analyzed volume of $63 \times 61 \times 75 \text{ nm}^3$ by APT. The APT results reveal a uniform distribution of alloying elements with near-equal atomic concentrations, as can be seen in Fig. 3(f). The FDA in Fig. 3(g) shows a good agreement between the experimental data and the binomial distribution [33,57]. The μ values, as discussed above, can be found in Table 1. Note that the APT-tip samples were extracted, adjacent to the grain-boundary region, to ensure a homogeneous elemental distribution, as secondary phases tend to precipitate along grain boundaries [58]. In short, the chemical segregation in the as-cast state was effectively eliminated by a systematic heat-treatment process, and the single-phase solid solution with the atomic-scale random elemental distribution was accomplished.

3.4. Mechanical properties at room and elevated temperatures

Fig. 4(a) presents the compressive engineering stress-strain curves of the as-cast and homogenization-treated NbTaTiV alloys at RT with a strain rate of $1\times 10^{-3}~\text{s}^{-1}$. The yield strengths (σ_y) of the as-cast and heat-treated samples are comparable (as-cast: 1236 MPa, and heat-treated: 1273 MPa) without the fracture occurring at a compressive strain limit of 30%. The compression experiments at RT were carried out, using the *in-situ* ND to investigate the deformation behavior during elastic and plastic deformations. Fig. 4(b) and (c) exhibit the corresponding lattice-strain evolutions of {110} and {200} planes along the loading

direction, as a function of the applied stress for the as-cast and homogenized samples, respectively. The lattice strains during loading, ε_{hkl} , are calculated from the shift of single-peak positions, using

$$\varepsilon_{hkl} = \frac{d_{hkl} - d_{hkl,0}}{d_{hkl,0}} \tag{1}$$

where d_{hkl} is the d-spacing obtained from the hkl diffraction at a given load, and $d_{hkl,0}$ refers to the value without the load. The lattice-strain evolution can provide the $\{hkl\}$ plane-specific lattice strain during deformation. Generally, the $\{110\}$ -oriented grains yield initially, because the $\{110\}$ orientation is preferred for the slip in the BCC structure, and then the additional load transfers to $\{200\}$ -oriented grains, resulting in the increase of the $\{200\}$ lattice strain, which is known as load sharing or partitioning [59]. Our results obtained from both the as-cast and homogenized samples show the similar load-sharing trend, as observed in the conventional BCC alloys. However, the slopes of $\{110\}$ and $\{200\}$ lattice strains increase during the loading to 750-850 MPa, and 900-1000 MPa, respectively, in the as-cast condition. In contrast, the slopes for the homogenized state maintain a linear response until 1100 MPa.

The lattice-strain evolutions for {110} and {200} grains reveal that the stress value for the elastic-plastic transition of the as-cast sample (~1000 MPa) is slightly lower than the homogenized one (~1100 MPa), which is consistent with the engineering stress-strain behavior [Fig. 4(a)]. Fig. 4(d) and (e) illustrate the variations in the normalized peak width (W/W_0) of $\{110\}$, $\{200\}$, $\{211\}$, and $\{310\}$ peaks as a function of engineering strain. Note that the reference peak width (W₀) was taken at the initial diffraction pattern (before the applied stress). For both conditions, no significant changes of peak widths were observed during elastic deformation. After yielding, however, the peak widths of the homogenized sample [Fig. 4(e)] increase more considerably than those of the as-cast one during plastic deformation. The width increase could be associated with the stress-induced heterogeneous substructure, such as distortion and twining [60,61]. However, based on our examination concerning the lateral surface of the 15% deformed specimens using SEM and EBSD as shown in Fig. 5(a-c), a number of slip bands are observed without the formation of twin bands. These results indicate that the plastic-deformation behavior is mainly dominated by the dislocation-slip mechanism, and during the deformation of

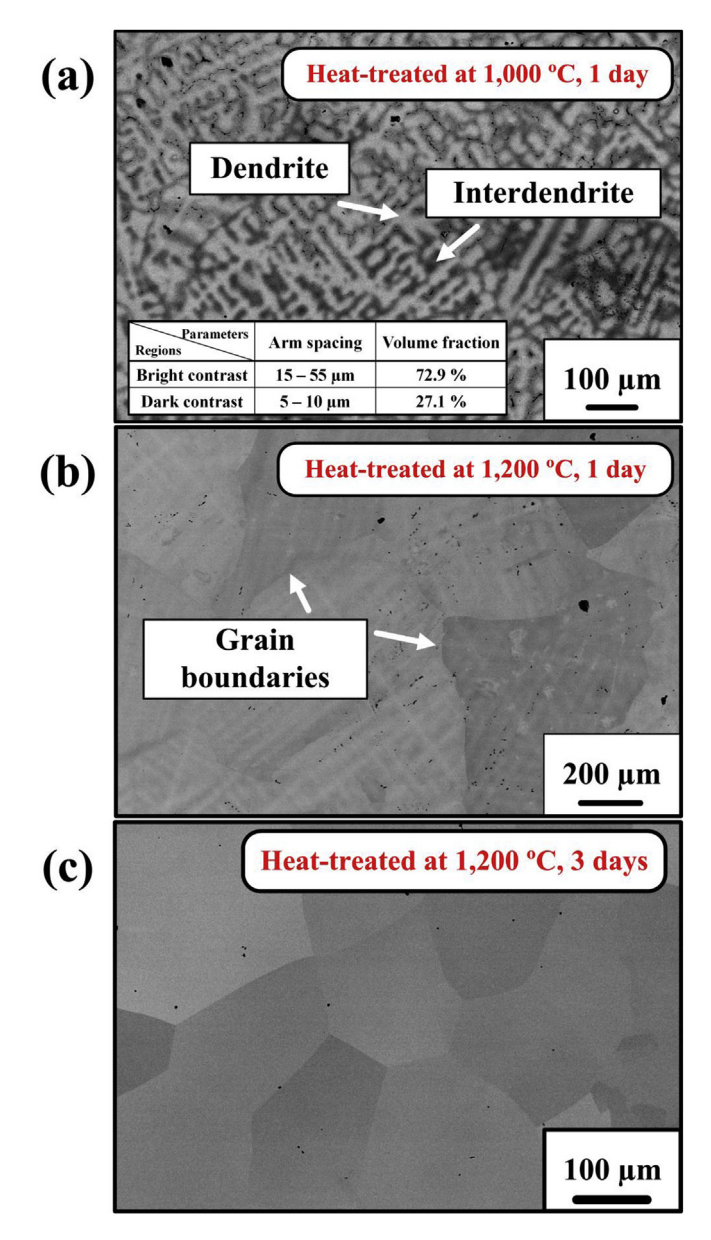


Fig. 3. Microstructural evolutions of the NbTaTiV alloy as a function of heat-treatment conditions, studied by SEM, ND, EBSD, and APT data. The SEM-BSE images of after-annealed samples at different temperatures and time periods: (a) 1000 °C for 1 day, (b) 1200 °C for 1 day, and (c) 1200 °C for 3 days, (d) Neutron-diffraction patterns of the NbTaTiV alloy after the heat treatment at 1200 °C for 3 days with the peaks indexed for a BCC structure. (e) EBSD-phase map of the homogenization-treated NbTaTiV alloy, and (f) A one-dimensional concentration-depth profile of all alloying elements taken along the black arrow for the homogenization-treated NbTaTiV alloy (top). Three-dimensional atom maps of individual elements (bottom) (g) FDA of constituent elements with a block size of 100 atoms for the homogenized NbTaTiV alloy. The solid lines are the binomial distribution, while dots are the observed experimental results.

the homogenized sample, more dislocations are produced as the plastic deformation proceeds.

The elevated-temperature compressive tests were performed up to 900 °C at a strain rate of $1\times 10^{-3}~s^{-1}$ for the homogenized alloy, and the stress-strain curves are illustrated in Fig. 6. As the temperature increases, the yield strength gradually decreases from 1273 MPa (RT) to 688 MPa (900 °C). Similar to the RT stress-strain curve, potent strain hardening is retained up to $800\,^{\circ}\text{C}$, but a slight reduction of the hardening capability is observed at $900\,^{\circ}\text{C}$. Note that the samples did not fracture up to a compressive strain limit of 30%. The values of the yield stress (σ_y) for the homogenized NbTaTiV alloy as a function of temperature are summarized in Fig. 6.

4. Discussion

4.1. Homogenization-treatment effects

The unique property of HEAs is obtained by increasing the configurational entropy, which introduces a simple solid-solution microstructure with severe lattice distortions caused by the random distribution of the constitutive elements that vary appreciably in size. Therefore, it is expected that the extent of the distortion effect is maximized when all the elements are homogenously distributed without the second-phase formation. In the present work, the fully-homogeneous single solid-solution microstructure in the NbTaTiV refractory HEA was achieved through

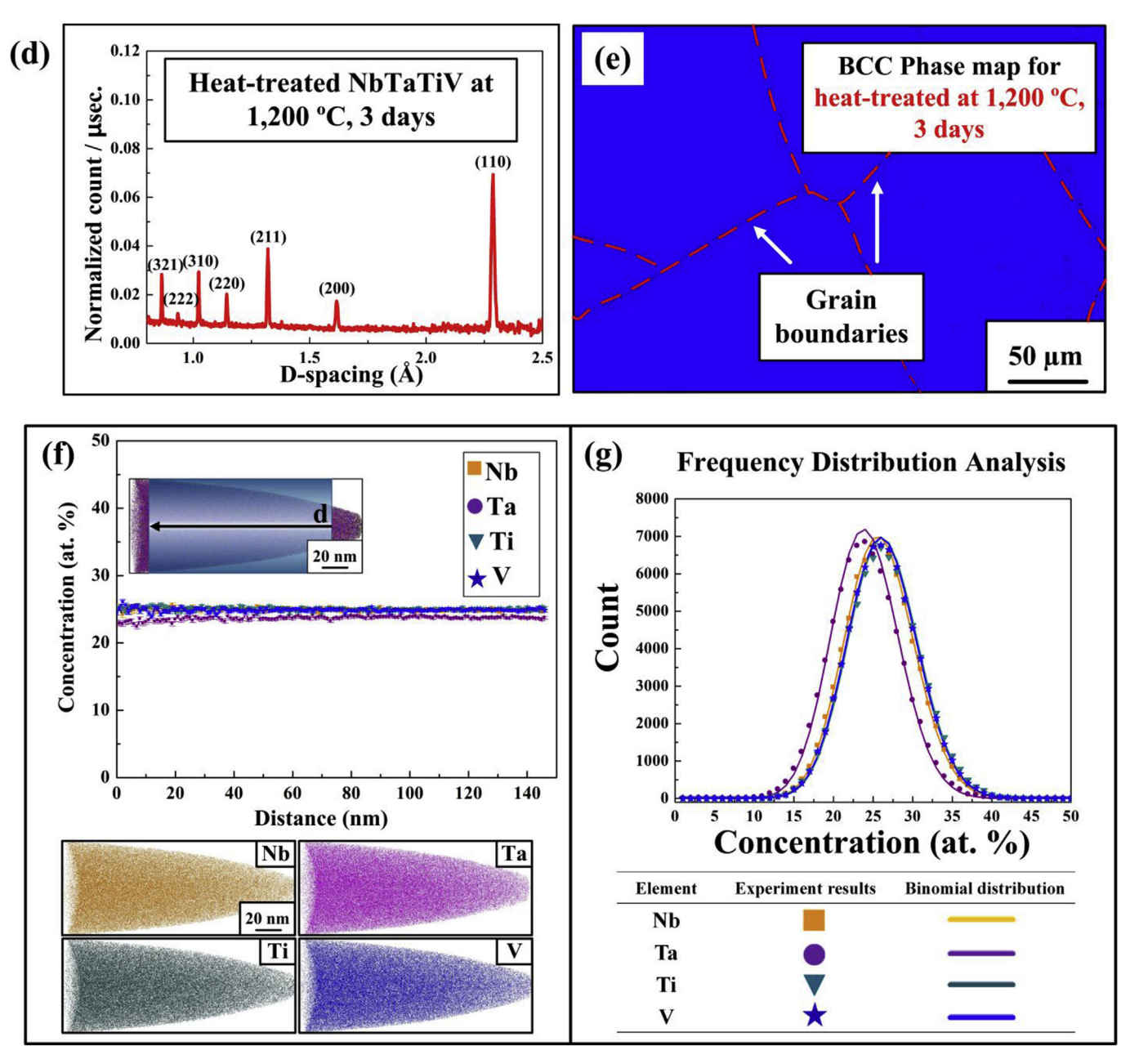


Fig. 3. (continued).

experimental and theoretical approaches. The clear microstructural evolution was captured from the chemically-inhomogeneous to simple BCC structures after the heat treatments. The chemical inhomogeneity is associated with the different melting temperature of each element in the alloy system. The segregation ratio, $S_R = (C_{dr})_i/(C_{idr})_i$, which considers the melting temperature of each constituent element [62] of the alloying component, was used to quantify the influence on micro-segregation. Here, the $(C_{dr})_i$ and $(C_{idr})_i$ are the atomic fractions of the element, i, in the dendritic and interdendritic regions, respectively. The calculated S_R values for Nb, Ta, Ti, and V in the as-cast sample based on the APT chemical analysis are 1.30, 2.35, 0.65, and 0.69, respectively. These values reflect that the Nb and Ta elements with high melting temperatures contribute mainly to the formation of dendritic regions, whereas the Ti and V elements with lower melting temperatures are preferentially distributed in the interdendritic regions. This calculation trend is consistent with the CALPHAD results (the inset in Fig. 1).

Based on the configurational-entropy approach, the chemical inhomogeneity in the as-cast sample is expected to reduce the distortion effect, as compared to the fully-homogeneous sample, which determines the extent of strengthening in the materials. However, the alloys in both states exhibit similar yield strengths. This trend could be due to other microstructural differences between the as-cast and heat-treated alloys, such as the grain size and possible presence of the residual stress during the casting process, as well as the compositional segregation making it difficult to clarify the influence of lattice distortion. Nevertheless, the variation at the distortion level during microstructural evolution could be determined by features obtained from neutron diffraction, such as lattice parameters and peak intensities. The lattice parameters of the as-cast sample and the heat-treated sample at 1200 °C for 3 days were determined from the ND patterns, using a single-peak fitting approach [63], and the averaged lattice parameters from the peaks observed were estimated to be $3.2372 \pm 0.0002 \,\text{Å}$ and

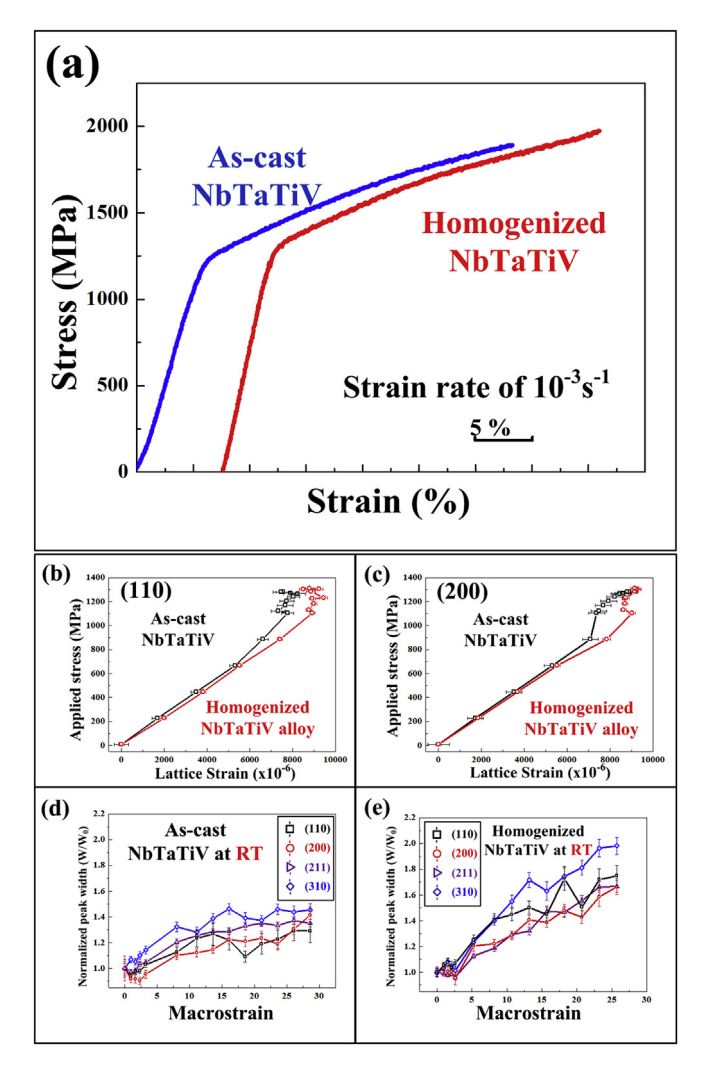


Fig. 4. Comparison of mechanical properties and *in-situ* neutron-diffraction data of the as-cast and homogenization-treated NbTaTiV. (a) Engineering compressive stress-strain curves of the as-cast and homogenization-treated NbTaTiV at room temperature. Evolution of lattice strains for (b) [110] (c) [200] oriented planes in ascast (black line) and homogenization-treated (red line) alloys as a function of applied stress. Evolution of normalized peak widths as a function of macro-strain for (d) As-cast, and (e) Homogenization-treated NbTaTiV HEAs. (For interpretation of the references to colour in this figure legend, the reader is referred to the Web version of this article.)

 3.2318 ± 0.0001 Å, respectively. A theoretical crystal-lattice parameter (a_{mix}) of the NbTaTiV alloy can be estimated with the rule of mixtures approach:

$$\mathbf{a}_{mix} = \sum_{i=1}^{n} c_i a_i \tag{2}$$

where n is the number of alloy components, c_i is the atomic fraction of the ith element, and a_i is the lattice parameter of the ith element. The lattice parameters measured for both as-cast and homogenized samples are slightly different with those acquired from the rule of mixtures (3.2342 Å), which could indicate lattice distortions in both cases

4.2. Quantitative determination of lattice distortion via experiments and calculations

Lattice distortion, which essentially originates from the atomic-

size mismatch in an alloy, constitutes one of the main features distinguishing HEAs from other metallic materials [4]. Importantly, lattice distortion affects the deformation mechanism as well as the mechanical properties of HEAs [30,31,64]. For example, severe lattice distortions produce unconventional dislocation lines in HEAs, leading to a distinct deformation mechanism in metallic materials [65,66]. These lattice distortions also introduce energy barriers against dislocation motions and serve as a strengthening mechanism [67]. Many properties of solid-solution HEAs, e.g., the phase stability and atomic-level stresses, are found to be correlated with the overall atomic-size mismatch [68,69].

There are experimental and theoretical reports regarding the influence of the lattice distortion on the diffraction-peak intensities in HEAs [30,31]. Specifically, the Cu-Ni-Al-Co-Cr-Fe-Si HEAs exhibit a considerable reduction in the XRD or ND intensities with the increase of the number of additional principal elements [31]. The peak intensities of neutron diffraction are closely related to the local chemical ordering/disordering in the lattice-distorted singlephase HEAs. During the neutron-beam irradiation, severe neutron scattering occurred on the rough diffraction planes, which is induced by significant lattice distortions, and it is expected to weaken the detectable diffraction signal. Similar to thermal effects, the atomic deviation from neutral positions (structural distortion) gives rise to the substantial deviation of the crystallization integrity, and, thus, an enhanced scattering effect. Thus, it results in simplified diffraction patterns and depressed peak intensities [31]. In the present study, the ND results show that the intensity of the {110} peaks for the homogenized sample is reduced by approximately 27%, as compared to the as-cast condition. Note that the diffraction peaks are fitted by the single-peak fitting method and, then, divided by the proton charge to conduct the precise comparison of peak heights. It can be deduced that the significant chemical inhomogeneity in the as-cast sample could induce the local chemical ordering, which leads to higher peak intensities. The evolutions of lattice strains and normalized peak widths during deformation, obtained by in-situ neutron studies, indicate that the slips of the as-cast alloy in the {110} and {200} oriented planes occur earlier than the homogenization-treated alloy, and a high density of dislocations is formed during plastic deformation. These distorted lattices induce the formation of local elastic-stress fields. During deformation, mobile dislocations could interact with the local elastic-stress fields. These stress fields could hinder the dislocation movements, which accounts for the high amounts of dislocations during plastic deformation [70].

Recently, Toda-caraballo et al. developed the strengthening theories to evaluate solid-solution strengthening in multicomponent alloy systems [71]. For solid-solution strengthening of metallic solid solutions originates from the elastic interactions between local stress fields of solute atoms and those of dislocations [67,72]. The interaction force (F) can be estimated as

$$F = Gb^2 \delta = Gb^2 [\beta \delta_a + \delta_G] \tag{3}$$

where $\delta_a = \frac{1}{a} \frac{da}{dc}$, $\delta_G = \frac{1}{G} \frac{dG}{dc}$, G is the shear modulus of the alloy, b is the magnitude of the Burgers Vector, and β is a constant, which is related with the difference in the interaction forces between screw and edge dislocations and the local stress field caused by solute atoms [71]. Typically, β is 2–4 for screw dislocations and \geq 16 for edge dislocations, respectively [71–73]. In the consideration of the ductility feature of the presently-studied BCC alloy, it is likely that a mixture of edge and screw dislocations is present, and thus, the β was determined to be 9 [13,74]. In a concentrated solid solution, the solute induced stress, $\Delta \sigma$, can be expressed as:

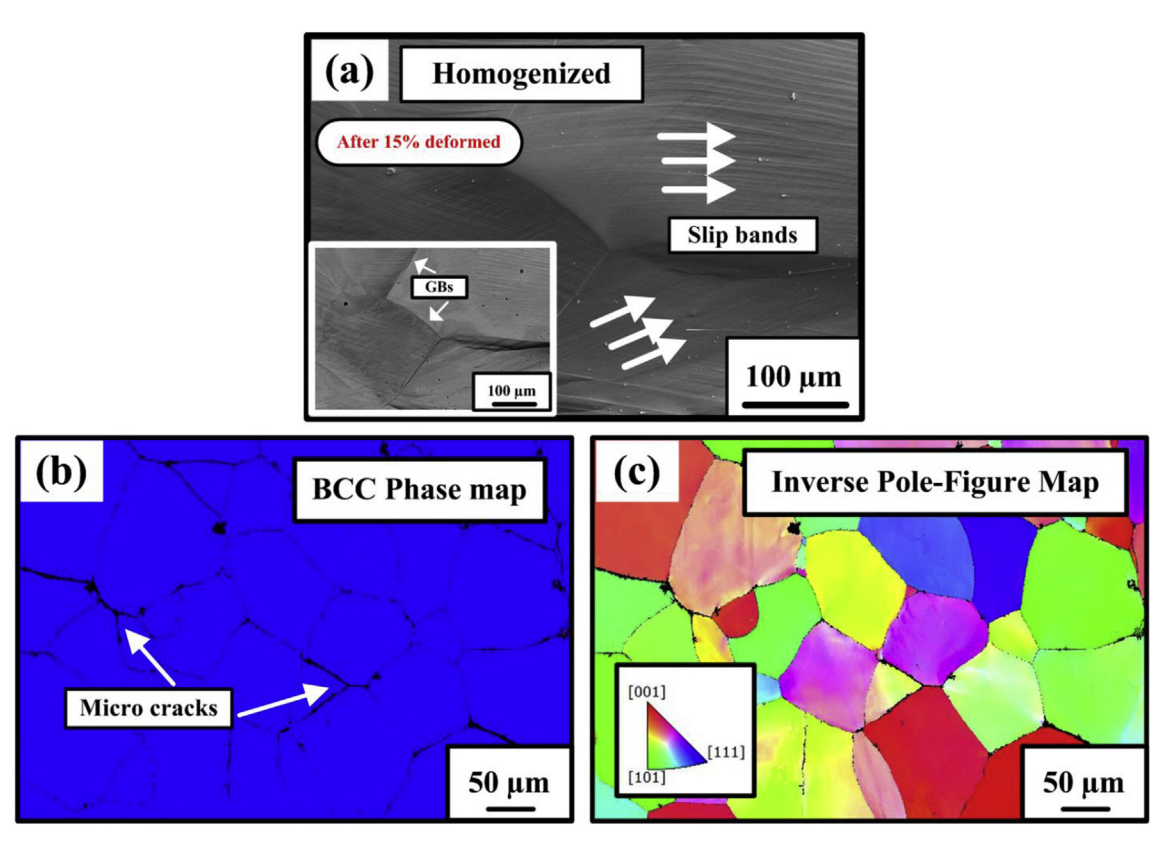


Fig. 5. SEM and EBSD images of the deformed lateral surface. (a) SEM micrograph of the homogenization-treated alloy after 15% deformation. (b and c) The EBSD phase and inverse pole-figure mapping images of the 15%-deformed homogenized NbTaTiV at room temperature. The SEM micrograph of the 15%-deformed homogenized sample shows a large density of slip bands that were nonuniformly oriented within different grains formed during plastic deformation. Furthermore, no strain-induced phase transformation was found to occur during compression testing, i.e., the single BCC solid-solution phase is observed on the phase map, and other deformation bands, such as local twin bands, were not observed from EBSD analyses.

$$\Delta\sigma = \frac{AF^{4/3}c^{2/3}E_L^{-1/3}}{b^2} \tag{4}$$

where A is a dimensionless material constant, c is a solute concentration, and E_L is the dislocation-line tension.

In the case of the single solid-solution phase HEA, the elastic and atomic-size mismatches are major factors for the solid-solution strengthening, which can be expressed as [13]:

$$\Delta\sigma_{\rm S} = \Delta\sigma_{\rm q} + \Delta\sigma_{\rm G} \tag{5}$$

where $\Delta\sigma_a$ and $\Delta\sigma_G$ are the strengthening contributions from the atomic-size mismatch (lattice distortion), and elastic-modulus mismatch (modulus distortion), respectively. According to Eqs. (3) and (4), the solute-induced stress with the consideration of the lattice distortion and modulus distortion can be expressed as [75]:

$$\Delta \sigma_{a(G)} = A'G \delta_{a(G)i}^{4/3} c_{a(G)i}^{2/3}$$
 (6)

where $A^{'}$ is a material-dependent dimensionless constant of the order of 0.04, G is the shear modulus of the alloy, which is estimated to be 49.5 GPa using the rule of mixtures, δ_i is the estimated average difference of the atomic size or shear modulus, and c_i is the solute concentration [74,75]. In case of a single BCC phase HEA, the δ_{ai} and δ_{Gi} in the adjacency of an element, i, are evaluated as averages of the atomic-size and modulus differences of this element with its neighbors, respectively,

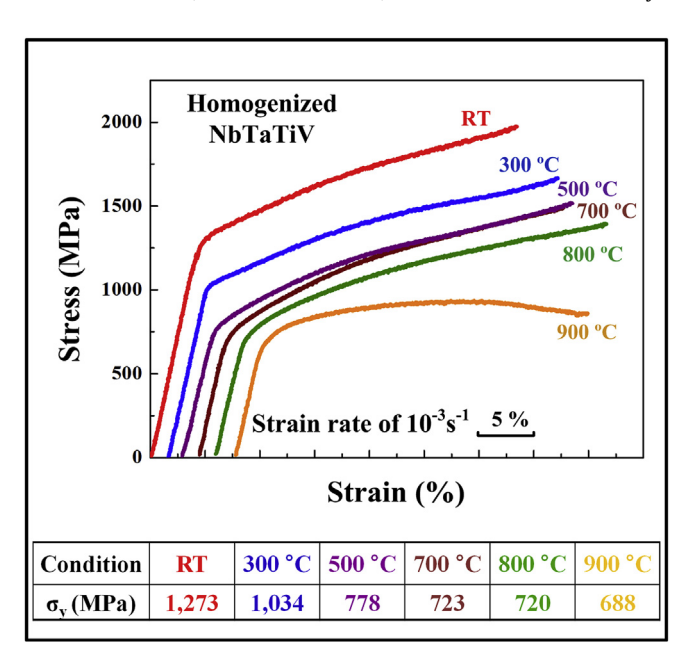


Fig. 6. Mechanical properties for NbTaTiV at elevated temperatures. Compressive engineering stress-strain curves and a summary of compression-yield strength (σ_y) for the homogenization-treated NbTaTiV alloy obtained at room temperature, 300 °C, 500 °C, 700 °C, 800 °C, and 900 °C, respectively.

$$\delta_{ai} = \frac{9}{8} \sum c_j \delta_{aij} \tag{7}$$

Table 2
The theoretical parameters ($Å^3$) of the six binary systems. A calculated volume before and after alloying for six binary systems, variation of volume, ΔV, and average of the volume difference, ΔV_{ii} , in the supercell.

| Parameters | Materials | Materials | | | | | |
|--------------------------|-----------------------------------|------------------|----------------------------------|-----------------------------------|----------------------------------|----------------------------------|--|
| | Nb ₅₀ Ta ₅₀ | $Nb_{50}Ti_{50}$ | Nb ₅₀ V ₅₀ | Ta ₅₀ Ti ₅₀ | Ta ₅₀ V ₅₀ | Ti ₅₀ V ₅₀ | |
| Volume (Before alloying) | 294.17 | 284.45 | 256.31 | 284.34 | 255.03 | 244.89 | |
| Volume (After alloying) | 294.08 | 284.72 | 254.32 | 285.04 | 254.64 | 245.28 | |
| ΔV | 0.0900 | - 0.2700 | 1.9900 | -0.7000 | 0.3900 | -0.3900 | |
| ΔV_{ij} | 0.0113 | -0.0338 | 0.2488 | -0.0875 | 0.0488 | -0.0488 | |

$$\delta_{Gi} = \frac{9}{8} \sum c_j \delta_{Gij} \tag{8}$$

where $\delta_{aij} = 2(r_i - r_j)/(r_i + r_j)$, $\delta_{Gij} = 2(G_i - G_j)/(G_i + G_j)$, G_i and G_j are the shear moduli of ith and jth elements, respectively, and G_j is the atomic fraction of jth element in the alloy.

According to the above equation, the strengthening components in the NbTaTiV alloy due to the lattice and modulus distortions are estimated to be $\Delta\sigma_a\approx 431$ MPa, and $\Delta\sigma_G\approx 227$ MPa, respectively. This result indicates that the lattice distortions are likely to be the dominant strengthening factor rather than modulus distortions in this alloy system.

From this point of view, one can point out that the quantitative as well as qualitative measurement of lattice distortions in the homogenized alloy is apparently important for understanding the strengthening mechanism. Yeh et al. [31] suggested the mathematical parameters of the distortion effect from the x-ray diffraction (XRD) structure factor of $\overline{F}_{hkl}^{T,D} = F_{hkl} \exp(-M^T - M^D)$, which is formulated by the combination of the Debye-Waller temperature

factor,
$$M^T = 8\pi^2 (\overline{u}^2)^T \left(\frac{\sin \theta}{\lambda}\right)^2$$
, and lattice-distortion factor, M^D ,

where θ and λ are the angle and wavelength of the incident x-ray beam, respectively. This thermal factor is remarkably associated with the vibration amplitude of atoms, \overline{u}^T . Similar to the vibrational amplitude of atoms caused by thermal effects, the lattice-distortion factor, M^D , is formulated as:

$$M^{D} = 8\pi^{2} \left(\overline{u}^{2}\right)^{D} \left(\frac{\sin\theta}{\lambda}\right)^{2} \tag{9}$$

In this factor, which is modified from M^T , the deviation displacement of atoms due to the intrinsic lattice distortion, \overline{u}^D , is the major effective term to determine M^D . The \overline{u}^D can be expressed by the following equation:

$$\overline{u}^{D} = \sqrt{\sum_{i}^{n} \left(d_{i}^{eff} - \overline{d}\right)^{2}}$$
 (10)

where d_i^{eff} is the effective lattice constant of the ith element, and \overline{d} is the average lattice constant of n elements, which are obtained from the atomic size of the incorporated elements related to the crystal structure. The effective lattice constant, d_i^{eff} , is calculated by:

$$d_i^{eff} = \sum_{i}^{n} f_j \left(1 + \frac{\Delta V_{ij}}{V_i} \right)^{1/3} d_i \tag{11}$$

where f_j is the atomic fraction, V_i is the atomic volume, d_i is the lattice constant of the ith element, ΔV_{ij} is the atomic-volume change of the ith element dissolved into the jth element, respectively. According to Eq. (6), the intrinsic lattice distortions due to

the incorporation of different size elements were calculated, using the first-principles method. The BCC NbTaTiV HEAs were modeled through the special quasi-random-structure (SQS) [76] method. Here, the intrinsic lattice distortion of the NbTaTiV alloy at zero temperature is calculated. The f_i is set to 0.25 because there are four elements, in which the composed elements are equally distributed in the HEA alloy. To calculate ΔV_{ij} and V_i , six kinds of binary systems need to be constructed, including A₅₀B₅₀, which denote the systems containing A and B, two of the four elements. A supercell containing 16 atoms is employed to construct the binary systems through SQS, and the lattice vectors of the supercell are defined as $a = 1 \overline{1} 1$, b = $1\overline{1}\overline{1}$. and c = 220. The volumes of the six binary systems are listed in Table 2. The volume before alloying denotes the sum volume of all the atoms in the supercell. To calculate the volume of supercells, one needs to multiply the number of atoms by the atomic volume in Table 3. The volume after alloying denotes that of the supercell after optimization. Then the total volume change, ΔV , can be obtained by $\Delta V = V$ (after alloying) - V (before alloying). Also the average atomic-volume differences, ΔV_{ii} , can be calculated through $\Delta V_{ii} = \Delta V/N$. Here N is equal to 8, since it corresponds to half of the number of atoms in the supercell.

According to Eqs. (5) and (6), the lattice-distortion parameters (\overline{u}^D) are calculated and listed in Table 3. For the quantitative comparison with the experimental result, the atomic fraction, which is obtained by the APT measurement, and the lattice parameter, which is acquired from the neutron-diffraction pattern, is replaced in f_j and \overline{d} factors, respectively. The obtained parameter, applying these experimentally-measured values, 0.2373 Å, is fairly close to the theoretically-calculated parameter (0.2344 Å) of the lattice distortion (\overline{u}^D) . The detailed values of lattice constants and lattice distortions are illustrated in Table 3. It indicates that the homogenization treatment promotes the rearrangement of atoms as a random distribution. Hence, the crystalline lattice is distorted as the predicted value of the theoretical calculation with the

Table 3 Theoretical calculations and experimental results of lattice distortions. Effective lattice constant (d_i^{eff}) of each element, lattice constant (\overline{d}) , and lattice-distortion parameter $(\overline{\mu}^D)$ of theoretically-calculated results in comparison to the experimental data. Note that the experimental results are calculated, based on the chemical composition, which is obtained from the APT measurements and lattice constants that are obtained through neutron diffraction.

| Parameters | Elements | | | | |
|---|-------------|--------|--------|--------|--------|
| | Condition | Nb | Ta | Ti | V |
| Atomic Volume (Å ³) | _ | 18.36 | 18.40 | 17.23 | 13.43 |
| Atomic Fraction (%) | Calculation | 0.250 | 0.250 | 0.250 | 0.250 |
| | Experiment | 0.249 | 0.236 | 0.251 | 0.250 |
| $d_i^{eff}(A)$ | Calculation | 2.8613 | 2.8597 | 2.8611 | 2.6263 |
| -1 () | Experiment | 2.8558 | 2.8578 | 2.8563 | 2.6194 |
| \overline{d} (Å) | Calculation | 2.8021 | | | |
| | Experiment | 2.7988 | | | |
| $\overline{\mu}^{\mathbf{D}}(\mathring{A})$ | Calculation | 0.2344 | | | |
| , , , | Experiment | 0.2373 | | | |

homogenization treatment.

4.3. Quantitative determination of lattice distortion via first-principles calculations

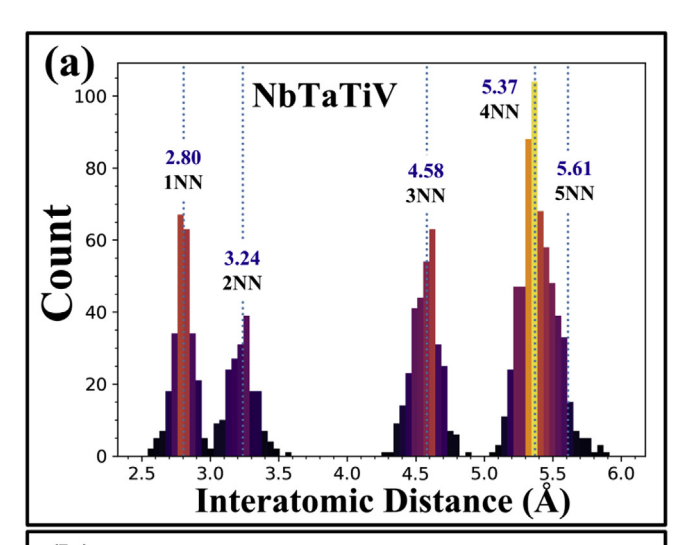
The mean-field lattice-distortion parameter is somewhat ambiguous in determining the local atomic displacement. To quantitatively understand the local lattice distortion of the BCC NbTaTiV HEA system, the distribution of atomic distances in a relaxed 64-atom NbTaTiV SQS was analyzed and shown in Fig. 7(a). It illustrates that the interatomic distance of all nth nearestneighboring (NN) pairs extends over a wide range, suggesting that many of the atoms deviate profoundly from their ideal lattice sites, leading to a severe local lattice distortion in this alloy system. The average interatomic distances of atomic pairs are r = 2.80, 3.23, 4.57, 5.42, and 6.47 Å for the first to fifth NN pairs, respectively. The effects of the local atomic relaxation can be excluded if we fix the atomic positions at the BCC lattice and only optimize the volume of the SQS. In such a case, the interatomic distances, rather than showing a wide spread, exhibit single values with r = 2.80, 3.24, 4.58, 5.37, and 5.61 Å for the first to fifth NN pairs. For the shortrange pairs, the average NN distances from the SQS are similar to the ideal BCC lattice. However, the deviation in average interatomic distances from an ideal BCC lattice for the 4NN and 5NN is noticeable. These results suggest that while the BCC lattice is maintained on average for the NbTaTiV HEA, a severe lattice distortion is predicted to be noticeable over longer ranges of atomic

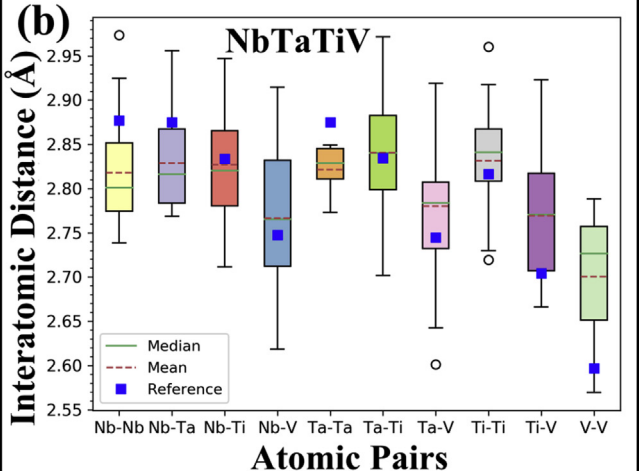
The BCC NbTaTiV system has ten different types of atomic pairs, i.e., the homoatomic pairs of Nb-Nb, Ti-Ti, Ta-Ta, and V-V, and the heteroatomic pairs of Nb-Ti, Nb-Ta, Nb-V, Ti-Ta, Ti-V, and Ta-V. Fig. 7(b) presents the NN interatomic distance of the aforementioned pairs in the SQS after the structural optimization. Additional DFT calculations were performed for the homoatomic and heteroatomic pairs with BCC and B2 crystal structures, respectively, to obtain the reference bond length for the interatomic pairs. These calculations provide comparable bond lengths for the atomic pairs in the BCC HEA. The mean and median of the interatomic distance of each pair are also shown in Fig. 7(b). The interatomic distance of all 1NN pairs spreads in wide ranges. Considering both the range of the interatomic distances and the mean value of a pair, a large number of atoms in the SQS shift strongly away from their ideal lattice sites, indicating a severe local lattice distortion in the NbTaTiV system. The lattice distortions can be defined as the change of the bond length with respect to the reference bond length:

$$Lattice \ distortion = \frac{|d_i - d_r|}{d_r} \times 100 \tag{12}$$

where d_i is the interatomic distance of a pair in the relaxed SQS, and d_r is the interatomic distance obtained for a pair with a BCC or B2 structure. Using this formula, the largest lattice distortion pairs are V–V and Ti–Ti, which are 4.7% and 5.1%, respectively. Among the heteroatomic pairs, the largest lattice distortions are the Nb–V and Ti–V pairs with a lattice distortion of 6.1% and 8.1%, respectively.

Fig. 7(b) illustrates how likely an atomic pair is compressed or elongated in the HEA. When the median bond length is less than the reference bond length of a pair, e.g., Nb—Nb, the bond is more likely to be under compression. The homoatomic pairs between Nb—Nb and Ta—Ta, the largest atoms of the HEA are mostly compressed, while the pairs of V—V, the smallest atom of the HEA are mostly elongated. On the other hand, in heteroatomic pairs, Ti atoms in combination with Nb and Ta appear to be balanced with their neighboring atoms on average. The heteroatomic pairs, with





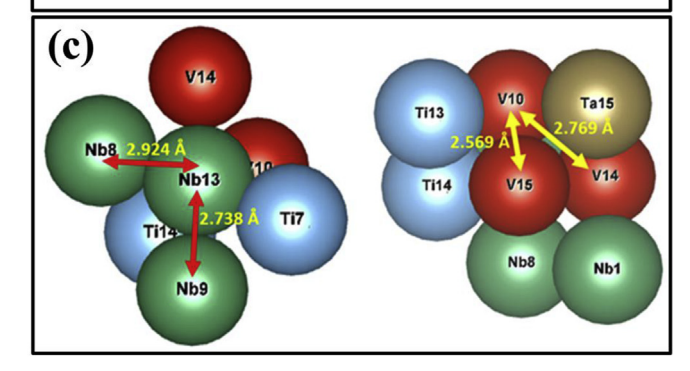


Fig. 7. First-principles calculation data. (a) Distribution of the interatomic distances for the first to fifth nearest neighbors (NN) of the BCC NbTaTiV HEA calculated from the optimized SQS. The blue dashed lines show the average interatomic distances for the first to fifth NNs, and (b) Box plot presenting the distribution of interatomic distances of 1NN bonds in the SQS for the BCC NbTaTiV HEA. The box presents the first and third quartiles of the bond lengths for a type of atomic bonds. The whisker extends to either the 1.5 interquartile ranges or the maximum and minimum values. The median and mean for each type of atomic bonds exhibit as the green solid line and red dashed line, respectively. The reference bond lengths, calculated from comparable BCC structures for the homoatomic pairs and B2 structures for the heteroatomic pairs, are shown in blue squares. (c) Two different locally-relaxed atomic structures of the BCC NbTaTiV HEA. The shortest and longest bond lengths of the Nb—Nb and V-V pairs for the first nearest neighbors in the supercells with the SQS model. (For interpretation of the references to colour in this figure legend, the reader is referred to the Web version of this article.)

the V atoms, show mostly elongation in their bond lengths. The compression/tension behavior in the bond lengths can be referred to the local environment of a pair, where placing some of the atoms in its neighborhood induces compression or tension to its bond. For example, while most of the Nb—Nb pair bonds are under compression in the HEA system, some of the Nb—Nb pair bonds are elongated due to the existence of V atoms in its first nearest neighboring environment as shown in Fig. 7(c). In addition to the difference in the atomic size, the change in the bond length of the HEA is also related to the chemical interactions among the principal elements.

4.4. Comparison of the temperature dependence of yield strengths

Fig. 8 shows the yield strengths of the NbTaTiV refractory HEA and two reported refractory HEAs [11], and conventional alloys, such as the Al-based alloy [77], Ti-based alloy [78], and Ni-based superalloys [11] at high temperatures. Compared with refractory HEAs, other alloys show a drastic decrease of the yield strength at certain temperatures. The Inconel 718, which maintains higher yield strengths at elevated temperatures, as compared with other conventional alloys, exhibits a rapid decline of the yield strength around 700 °C. However, the refractory HEAs, NbTaTiV, MoNbTaW, and MoNbTaVW, present no substantial reduction of yield strengths as a function of temperatures. Besides, the values of yield strengths for NbTaTiV and MoNbTaVW alloys are much higher than other alloys at the temperatures above 800 °C. The ability of the material to retain its strength at high temperatures could be the consequence of the sluggish diffusion [79]. The nature of the slower diffusion of elements at higher temperatures in the single BCC structural refractory HEAs may arise from its structure, which consists of multi-principal elements (that possess the high melting temperature and different atomic radii) [79]. Thus, these trends can lead to the strong resistance of high-temperature softening.

5. Conclusions

Overall, this comprehensive study provides a method of the design and development of the single-phase BCC solid-solution phase refractory HEA, using an integrated experimental and theoretical thermodynamic-calculation approach. The results of the APT measurement and the neutron-diffraction patterns indicate that the structure is composed of a single-phase BCC solid solution as well as a homogeneous elemental distribution with equimolar ratios. Furthermore, the mechanical-test results of the

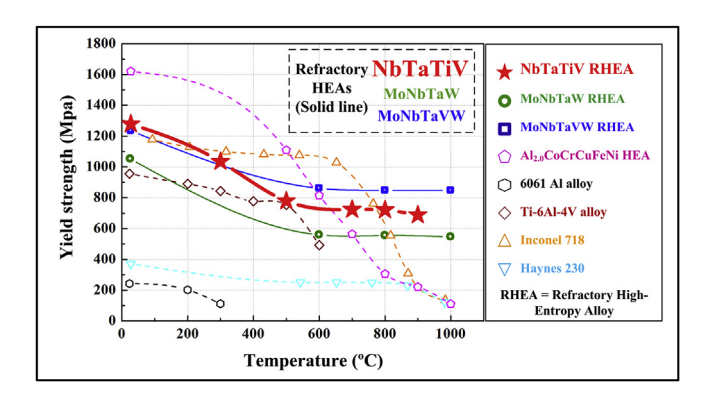


Fig. 8. Comparison of the temperature dependence of yield strengths. Yield strengths of the NbTaTiV alloy and two reported refractory HEAs (MoNbTaW and MoNbTaVW), conventional HEA (Al_{2.0}CoCrCuFeNi), Al-based alloy (6061 Al alloy), Tibased alloy (Ti-6Al-4V alloy), and Ni-based superalloys (Inconel 718 and Haynes 230) as a function of temperature [10,72,73].

homogenization-treated sample show the excellent yield strength and plasticity at RT as well as elevated temperatures. The dominant strengthening mechanism was found to be solid-solution hardening, which stems from the distortion of the crystalline lattice during deformation. It is thought that this strengthening mechanism induces slow elemental diffusion at high temperatures, which, consequently, leads to the strong resistance of hightemperature softening. The distorted lattice for this alloy system was quantitatively calculated by the mathematical computation and theoretical modeling, such as first-principles calculations. The results of the above modeling and analysis indicate that the local severe lattice distortions are induced, due to the atomic-size mismatch and local atomic interactions in the homogenizationtreated NbTaTiV refractory HEA. These results provide (1) a novel alloy-design strategy, (2) a fundamental understanding of the lattice-distortion effect on mechanical properties, and (3) a road map to produce better materials for high-temperatures applications.

Competing financial interests

The authors declare that they have no competing financial interests.

Author contributions

All authors contributed extensively to the work presented in this manuscript. C.L., P.K.L., R.F., P.C., and J.B. performed the scanning-electron-microscopy, electron back-scattered diffraction, in-situ neutron, and mechanical tests. C.L., G.S., and P.K.L. wrote the main manuscript and supplementary information. M.C.G. conducted the calculation of the phase diagram and wrote the computational prediction parts in the main manuscript. Y.C., K.A., and H.C. performed the in-situ neutron experiments and analyzed data. W.G. and J.P. carried out and analyzed the atom-probe-tomography experiments. S.L., A.T.S., A.H., and W.C. conducted the first-principles calculation and wrote the calculation parts in the main manuscript. All authors discussed the results and implications and commented on the manuscript at all stages.

Acknowledgments

The research is supported by the U.S. Army Office Project (W911NF-13-1-0438) with the program managers, Michael P. Bakas and David M. Stepp, and the material was developed. Peter K. Liaw also thanks the support from the National Science Foundation (DMR-1611180 and 1809640) with the program director, Gary Shiflet and Diana Farkas, and the neutron work was conducted. C. Lee would like to acknowledge the partial support from the Center of Materials Processing with Prof. Claudia Rawn as the director, a Tennessee Higher Education Commission (THEC) Center of Excellence located at The University of Tennessee, Knoxville. The CAL-PHAD modeling work was carried out to support the Cross-Cutting Technologies Program at the National Energy Technology Laboratory (NETL) — Strategic Center for Coal, managed by Robert Romanosky (Technology Manager) and Charles Miller (Technology Monitor). The research was executed through the NETL's Office of Research and Development's Innovative Process Technologies (IPT) Field Work Proposal. Research performed by the AECOM staff was conducted under the RES contract, DE-FE-0004000. The APT measurements were performed as a part of a user proposal at the ORNL's Center for the Nanophase Materials Science (CNMS), which is a DOE Office of Science User Facility (JDP and WG). A portion of research at the ORNL's Spallation Neutron Source was sponsored by the Scientific User Facilities Division, Office of Basic Energy

Sciences, U.S. Department of Energy. The first-principles research is also supported by the City University of Hong Kong (Grant No. 9610336), National Natural Science Foundation of China (NSFC) (Grant No. 11605148), and Research Grants Council of the Hong Kong Special Administrative Region, China (Project No. CityU 21202517) Disclaimer: The computational-modeling work presented in the paper was funded by the Department of Energy, National Energy Technology Laboratory, an agency of the United States Government, through a support contract with AECOM. Neither the United States Government nor any agency thereof, nor any of their employees, nor AECOM, nor any of their employees, makes any warranty, expressed or implied, or assumes any legal liability or responsibility for the accuracy, completeness, or usefulness of any information, apparatus, product, or process disclosed, or represents that its use would not infringe privately owned rights. Reference herein to any specific commercial product, process, or service by trade name, trademark, manufacturer, or otherwise, does not necessarily constitute or imply its endorsement, recommendation, or favoring by the United States Government or any agency thereof. The views and opinions of authors expressed herein do not necessarily state or reflect those of the United States Government or any agency thereof.

References

- Z. Li, K.G. Pradeep, Y. Deng, D. Raabe, C.C. Tasan, Metastable high-entropy dual-phase alloys overcome the strength-ductility trade-off, Nature 534 (2016) 227–231.
- [2] L.J. Santodonato, Y. Zhang, M. Feygenson, C.M. Parish, M.C. Gao, R.J. Weber, J.C. Neuefeind, Z. Tang, P.K. Liaw, Deviation from high-entropy configurations in the atomic distributions of a multi-principal-element alloy, Nat. Commun. 6 (2015) 5964.
- [3] Y. Zhang, Y.J. Zhou, J.P. Lin, G.L. Chen, P.K. Liaw, Solid-solution phase formation rules for multi-component alloys, Adv. Eng. Mater. 10 (6) (2008) 534–538.
- [4] Y. Zhang, T.T. Zuo, Z. Tang, M.C. Gao, K.A. Dahmen, P.K. Liaw, Z.P. Lu, Micro-structures and properties of high-entropy alloys, Prog. Mater. Sci. 61 (2014)
- [5] B. Gludovatz, A. Hohenwarter, D. Catoor, E.H. Chang, E.P. George, R.O. Ritchie, A fracture-resistant high-entropy alloy for cryogenic applications, Science 345 (6201) (2014) 1153–1158.
- [6] F. Otto, Y. Yang, H. Bei, E.P. George, Relative effects of enthalpy and entropy on the phase stability of equiatomic high-entropy alloys, Acta Mater. 61 (7) (2013) 2628–2638.
- [7] O. Senkov, J. Miller, D. Miracle, C. Woodward, Accelerated exploration of multi-principal element alloys with solid solution phases, Nat. Commun. 6 (2015) 6529.
- [8] M.C. Troparevsky, J.R. Morris, P.R. Kent, A.R. Lupini, G.M. Stocks, Criteria for predicting the formation of single-phase high-entropy alloys, Phys. Rev. X 5 (1) (2015), 011041.
- [9] B. Cantor, I. Chang, P. Knight, A. Vincent, Microstructural development in equiatomic multicomponent alloys, Mater. Sci. Eng. 375 (2004) 213–218.
- [10] O. Senkov, G. Wilks, D. Miracle, C. Chuang, P. Liaw, Refractory high-entropy alloys, Intermetallics 18 (9) (2010) 1758–1765.
- [11] O. Senkov, G. Wilks, J. Scott, D. Miracle, Mechanical properties of Nb₂₅Mo₂₅. Ta₂₅W₂₅ and V₂₀Nb₂₀Mo₂₀Ta₂₀W₂₀ refractory high entropy alloys, Intermetallics 19 (5) (2011) 698–706.
- [12] O. Senkov, J. Scott, S. Senkova, F. Meisenkothen, D. Miracle, C. Woodward, Microstructure and elevated temperature properties of a refractory TaNbHfZrTi alloy, J. Mater. Sci. 47 (9) (2012) 4062–4074.
- [13] O. Senkov, J. Scott, S. Senkova, D. Miracle, C. Woodward, Microstructure and room temperature properties of a high-entropy TaNbHfZrTi alloy, J. Alloy. Comp. 509 (20) (2011) 6043—6048.
- [14] K.M. Youssef, A.J. Zaddach, C. Niu, D.L. Irving, C.C. Koch, A novel low-density, high-hardness, high-entropy alloy with close-packed single-phase nanocrystalline structures, Mater. Res. Lett. 3 (2) (2015) 95–99.
- [15] M.C. Gao, B. Zhang, S. Guo, J. Qiao, J. Hawk, High-entropy alloys in hexagonal close-packed structure, Metall. Mater. Trans. 47 (7) (2016) 3322–3332.
- [16] Z. Zhang, M. Mao, J. Wang, B. Gludovatz, Z. Zhang, S.X. Mao, E.P. George, Q. Yu, R.O. Ritchie, Nanoscale origins of the damage tolerance of the high-entropy alloy CrMnFeCoNi, Nat. Commun. 6 (2015) 10143.
- [17] B. Gludovatz, A. Hohenwarter, K.V. Thurston, H. Bei, Z. Wu, E.P. George, R.O. Ritchie, Exceptional damage-tolerance of a medium-entropy alloy CrCoNi at cryogenic temperatures, Nat. Commun. 7 (2016) 10602.
- [18] Y. Jo, S. Jung, W. Choi, S. Sohn, H. Kim, B. Lee, N. Kim, S. Lee, Cryogenic strength improvement by utilizing room-temperature deformation twinning in a partially recrystallized VCrMnFeCoNi high-entropy alloy, Nat. Commun. 8 (2017) 15719.

- [19] H. Huang, X. Li, Z. Dong, W. Li, S. Huang, D. Meng, X. Lai, T. Liu, S. Zhu, L. Vitos, Critical stress for twinning nucleation in CrCoNi-based medium and high entropy alloys, Acta Mater. 149 (2018) 388–396.
- [20] F. Otto, A. Dlouhý, C. Somsen, H. Bei, G. Eggeler, E.P. George, The influences of temperature and microstructure on the tensile properties of a CoCrFeMnNi high-entropy alloy, Acta Mater. 61 (15) (2013) 5743-5755.
- [21] G.D. Sathiaraj, P.P. Bhattacharjee, Analysis of microstructure and microtexture during grain growth in low stacking fault energy equiatomic CoCrFeMnNi high entropy and Ni–60 wt.% Co alloys, J. Alloy. Comp. 637 (2015) 267–276.
- [22] S. Huang, W. Li, S. Lu, F. Tian, J. Shen, E. Holmström, L. Vitos, Temperature dependent stacking fault energy of FeCrCoNiMn high entropy alloy, Scripta Mater. 108 (2015) 44–47.
- [23] Y. Deng, C.C. Tasan, K.G. Pradeep, H. Springer, A. Kostka, D. Raabe, Design of a twinning-induced plasticity high entropy alloy, Acta Mater. 94 (2015) 124–133.
- [24] Z. Li, C.C. Tasan, H. Springer, B. Gault, D. Raabe, Interstitial atoms enable joint twinning and transformation induced plasticity in strong and ductile highentropy alloys, Sci. Rep. 7 (2017) 40704.
- [25] Z. Li, C.C. Tasan, K.G. Pradeep, D. Raabe, A TRIP-assisted dual-phase high-entropy alloy: grain size and phase fraction effects on deformation behavior, Acta Mater. 131 (2017) 323–335.
- [26] O. Senkov, S. Senkova, D. Miracle, C. Woodward, Mechanical properties of low-density, refractory multi-principal element alloys of the Cr-Nb-Ti-V-Zr system, Mater. Sci. Eng. 565 (2013) 51–62.
- [27] O. Senkov, S. Senkova, C. Woodward, Effect of aluminum on the microstructure and properties of two refractory high-entropy alloys, Acta Mater. 68 (2014) 214–228.
- [28] Y. Zou, H. Ma, R. Spolenak, Ultrastrong ductile and stable high-entropy alloys at small scales, Nat. Commun. 6 (2015) 7748.
- [29] J.-W. Yeh, S.-J. Lin, T.-S. Chin, J.-Y. Gan, S.-K. Chen, T.-T. Shun, C.-H. Tsau, S.-Y. Chou, Formation of simple crystal structures in Cu-Co-Ni-Cr-Al-Fe-Ti-V alloys with multiprincipal metallic elements, Metall. Mater. Trans. 35 (8) (2004) 2533–2536.
- [30] W. Guo, W. Dmowski, J.-Y. Noh, P. Rack, P.K. Liaw, T. Egami, Local atomic structure of a high-entropy alloy: an x-ray and neutron scattering study, Metall. Mater. Trans. 44 (5) (2013) 1994–1997.
- [31] J.-W. Yeh, S.-Y. Chang, Y.-D. Hong, S.-K. Chen, S.-J. Lin, Anomalous decrease in X-ray diffraction intensities of Cu–Ni–Al–Co–Cr–Fe–Si alloy systems with multi-principal elements, Mater. Chem. Phys. 103 (1) (2007) 41–46.
- [32] Y. Wu, Y. Cai, T. Wang, J. Si, J. Zhu, Y. Wang, X. Hui, A refractory Hf₂₅Nb₂₅Ti₂₅Zr₂₅ high-entropy alloy with excellent structural stability and tensile properties, Mater. Lett. 130 (2014) 277–280.
- [33] M. Yao, K. Pradeep, C. Tasan, D. Raabe, A novel, single phase, non-equiatomic FeMnNiCoCr high-entropy alloy with exceptional phase stability and tensile ductility, Scripta Mater. 72 (2014) 5–8.
- [34] N. Stepanov, N.Y. Yurchenko, V. Sokolovsky, M. Tikhonovsky, G. Salishchev, An AlNbTiVZr_{0.5} high-entropy alloy combining high specific strength and good ductility, Mater. Lett. 161 (2015) 136–139.
- [35] N. Stepanov, N.Y. Yurchenko, D. Shaysultanov, G. Salishchev, M. Tikhonovsky, Effect of Al on structure and mechanical properties of AlxNbTiVZr (x= 0, 0.5, 1, 1.5) high entropy alloys, Mater. Sci. Technol. 31 (10) (2015) 1184–1193.
- [36] S. Maiti, W. Steurer, Structural-disorder and its effect on mechanical properties in single-phase TaNbHfZr high-entropy alloy, Acta Mater. 106 (2016) 87–97.
- [37] M.C. Gao, D.E. Alman, Searching for next single-phase high-entropy alloy compositions, Entropy 15 (10) (2013) 4504–4519.
- [38] F. Zhang, C. Zhang, S. Chen, J. Zhu, W. Cao, U. Kattner, An understanding of high entropy alloys from phase diagram calculations, Calphad 45 (2014) 1–10.
- [39] R. Feng, M.C. Gao, C. Lee, M. Mathes, T. Zuo, S. Chen, J.A. Hawk, Y. Zhang, P.K. Liaw, Design of light-weight high-entropy alloys, Entropy 18 (9) (2016) 333
- [40] A. Zunger, S.-H. Wei, L. Ferreira, J.E. Bernard, Special quasirandom structures, Phys. Rev. Lett. 65 (3) (1990) 353.
- [41] B. Sundman, B. Jansson, J.-O. Andersson, The thermo-calc databank system, Calphad 9 (2) (1985) 153–190.
- [42] M.C. Gao, J.-W. Yeh, P.K. Liaw, Y. Zhang, High-entropy Alloys: Fundamentals and Applications, Springer, 2016.
- [43] C.A. Schneider, W.S. Rasband, K.W. Eliceiri, NIH Image to ImageJ: 25 years of image analysis, Nat. Methods 9 (7) (2012) 671.
- [44] D.J. Larson, T.J. Prosa, R.M. Ulfig, B.P. Geiser, T.F. Kelly, Local Electrode Atom Probe Tomography, Springer Science, New York, US, 2013.
- [45] K. Thompson, D. Lawrence, D. Larson, J. Olson, T. Kelly, B. Gorman, In situ site-specific specimen preparation for atom probe tomography, Ultramicroscopy 107 (2) (2007) 131–139.
- [46] K. An, H.D. Skorpenske, A.D. Stoica, D. Ma, X.-L. Wang, E. Cakmak, First in situ lattice strains measurements under load at VULCAN, Metall. Mater. Trans. 42 (1) (2011) 95–99.
- [47] X.-L. Wang, T. Holden, G.Q. Rennich, A. Stoica, P.K. Liaw, H. Choo, C.R. Hubbard, VULCAN—the engineering diffractometer at the SNS, Phys. B Condens. Matter 385 (2006) 673–675.
- [48] K. An, VDRIVE-data Reduction and Interactive Visualization Software for Event Mode Neutron Diffraction, ORNL Report No. ORNL-tm-2012-621, Oak Ridge National Laboratory, Oak Ridge, TN, 2012.
- [49] G. Kresse, J. Furthmüller, Efficient iterative schemes for ab initio total-energy

- calculations using a plane-wave basis set, Phys. Rev. B 54 (16) (1996) 11169.
- [50] P.E. Blöchl, O. Jepsen, O.K. Andersen, Improved tetrahedron method for Brillouin-zone integrations, Phys. Rev. B 49 (23) (1994) 16223.
- [51] G. Kresse, D. Joubert, From ultrasoft pseudopotentials to the projector augmented-wave method, Phys. Rev. B 59 (3) (1999) 1758.
- [52] J.P. Perdew, K. Burke, M. Ernzerhof, Generalized gradient approximation made simple, Phys. Rev. Lett. 77 (18) (1996) 3865.
- [53] H.J. Monkhorst, J.D. Pack, Special points for Brillouin-zone integrations, Phys. Rev. B 13 (12) (1976) 5188.
- [54] M. Gao, C. Carney, Ö. Doğan, P. Jablonksi, J. Hawk, D. Alman, Design of re-fractory high-entropy alloys, JOM (J. Occup. Med.) 67 (11) (2015) 2653–2669.
- [55] E. Scheil, Comments on the layer crystal formation, Z. Metallkd 34 (1942) 70–72.
- [56] M.K. Miller, Atom Probe Tomography: Analysis at the Atomic Level, Springer Science & Business Media, 2012.
- [57] M.P. Moody, L.T. Stephenson, A.V. Ceguerra, S.P. Ringer, Quantitative binomial distribution analyses of nanoscale like-solute atom clustering and segregation in atom probe tomography data, Microsc. Res. Tech. 71 (7) (2008) 542–550.
- [58] F. Otto, A. Dlouhý, K. Pradeep, M. Kuběnová, D. Raabe, G. Eggeler, E. George, Decomposition of the single-phase high-entropy alloy CrMnFeCoNi after prolonged anneals at intermediate temperatures, Acta Mater. 112 (2016) 40–52
- [59] S. Huang, D.W. Brown, B. Clausen, Z. Teng, Y. Gao, P.K. Liaw, In situ neutrondiffraction studies on the creep behavior of a ferritic superalloy, Metall. Mater. Trans. 43 (5) (2012) 1497–1508.
- [60] T. Ungár, J. Gubicza, G. Ribárik, A. Borbély, Crystallite size distribution and dislocation structure determined by diffraction profile analysis: principles and practical application to cubic and hexagonal crystals, J. Appl. Crystallogr. 34 (3) (2001) 298–310.
- [61] E. Francis, B. Grant, J.Q. da Fonseca, P. Phillips, M. Mills, M. Daymond, M. Preuss, High-temperature deformation mechanisms in a polycrystalline nickel-base superalloy studied by neutron diffraction and electron microscopy, Acta Mater. 74 (2014) 18–29.
- [62] N. Guo, L. Wang, L. Luo, X. Li, R. Chen, Y. Su, J. Guo, H. Fu, Effect of composing element on microstructure and mechanical properties in Mo–Nb–Hf–Zr–Ti multi-principle component alloys, Intermetallics 69 (2016) 13–20.
- [63] A. Larson, R. Von Dreele, GSAS General Structure Analysis System, LANSCE, MS-H805, Los Alamos National Laboratory, Los Alamos, 1998.
- [64] D. Miracle, O. Senkov, A critical review of high entropy alloys and related

- concepts, Acta Mater. 122 (2017) 448-511.
- [65] F. Granberg, K. Nordlund, M.W. Ullah, K. Jin, C. Lu, H. Bei, L. Wang, F. Djurabekova, W. Weber, Y. Zhang, Mechanism of radiation damage reduction in equiatomic multicomponent single phase alloys, Phys. Rev. Lett. 116 (13) (2016) 135504.
- [66] C. Lu, T. Yang, K. Jin, N. Gao, P. Xiu, Y. Zhang, F. Gao, H. Bei, W.J. Weber, K. Sun, Radiation-induced segregation on defect clusters in single-phase concentrated solid-solution alloys, Acta Mater. 127 (2017) 98–107.
- [67] R. Labusch, A statistical theory of solid solution hardening, Physica Status Solidi (B) 41 (2) (1970) 659–669.
- [68] Y. Ye, C. Liu, Y. Yang, A geometric model for intrinsic residual strain and phase stability in high entropy alloys, Acta Mater. 94 (2015) 152–161.
- [69] G. Sheng, C.T. Liu, Phase stability in high entropy alloys: formation of solid-solution phase or amorphous phase, Prog. Nat. Sci.: Mater. Int. 21 (6) (2011) 433–446.
- [70] Y. Zhang, X. Yang, P.K. Liaw, Alloy design and properties optimization of highentropy alloys, JOM (J. Occup. Med.) 64 (7) (2012) 830–838.
- [71] I. Toda-Caraballo, P.E. Rivera-Díaz-del-Castillo, Modelling solid solution hardening in high entropy alloys, Acta Mater. 85 (2015) 14–23.
- [72] R. Fleischer, Substitutional solution hardening, Acta Metall. 11 (3) (1963) 203–209
- [73] L. Gypen, A. Deruyttere, Multi-component solid solution hardening, J. Mater. Sci. 12 (5) (1977) 1028–1033.
- [74] H. Yao, J. Qiao, J. Hawk, H. Zhou, M. Chen, M. Gao, Mechanical properties of refractory high-entropy alloys: experiments and modeling, J. Alloy. Comp. 696 (2017) 1139–1150.
- [75] R. Arsenault, Treatise on Materials Science and Technology, vol. I, Plastic Deformation of Materials, 1975.
- [76] A. Van de Walle, P. Tiwary, M. De Jong, D. Olmsted, M. Asta, A. Dick, D. Shin, Y. Wang, L-Q. Chen, Z.-K. Liu, Efficient stochastic generation of special quasirandom structures, Calphad 42 (2013) 13–18.
- [77] C.-J. Tong, M.-R. Chen, J.-W. Yeh, S.-J. Lin, S.-K. Chen, T.-T. Shun, S.-Y. Chang, Mechanical performance of the Al_xCoCrCuFeNi high-entropy alloy system with multiprincipal elements, Metall. Mater. Trans. 36 (5) (2005) 1263–1271.
- [78] S. Zherebtsov, G. Salishchev, R. Galeyev, K. Maekawa, Mechanical properties of Ti-6Al-4V titanium alloy with submicrocrystalline structure produced by severe plastic deformation, Mater. Trans. 46 (9) (2005) 2020–2025.
- [79] K.-Y. Tsai, M.-H. Tsai, J.-W. Yeh, Sluggish diffusion in CO-Cr-Fe-Mn-Ni high-entropy alloys, Acta Mater. 61 (13) (2013) 4887-4897.